2024 IEEE International Conference on Robotics and Automation (ICRA 2024)
May 13-17, 2024. Yokohama, Japan

A Meter-scale Ornithopter Capable of Jumping Take-off

Wei Yan, Genliang Chen, Zhuang Zhang and Hao Wang

Abstract— **Flapping wing air vehicles(FWAV) or ornithopters are bio-inspired aerial robots that mimic the flying principles of insects and birds. Autonomous take-off is an important capability for FWAV to enhance its performance and extend its working time, which is equipped by almost every kind of bird. As a common method of take-off for birds, jumping take-off has a great ability to adapt to different terrain and high energy efficiency compared with running and rotor-based take-off. Despite recent research, there is no FWAV capable of jumping take-off to this day. In this paper, we present a process to realize the jumping take-off of a meter-scale FWAV from flat ground. To lower the mechanical complexity, we eliminate the design of traditional robotic legs. Instead, we realize steady standing through a tripod-like structure that consists of two wings and a jumping mechanism. Two flapping wings are directly driven by two independent servos. Three carbon fiber springs are employed to build a lightweight jumping module with high elastic energy. We build the dynamic model to analyze the aerodynamic effect during the jumping phase and realize a stable transition to flapping flight. This work lays the foundation for outdoor flight without human assistance.**

I. Introduction

In nature, birds have perfected the art of autonomous take-off, a skill that is crucial for their survival and daily activities. Whether landing to rest, hunt, or survey their environment, birds often need to take off in unpredictable and complex terrain. Similarly, for bio-inspired aerial robots, particularly Flapping-Wing Aerial Vehicles (FWAV), the ability to take off autonomously offers a myriad of advantages. In FWAVs, unexpected landings may occur due to collisions in outdoor environments. An autonomous take-off capability allows these vehicles to recover quickly. In addition, given the constraints posed by battery energy density, FWAV can land for a relaxation beyond working time to prolong operational time.

Except for some small-scale birds like hummingbirds that can realize vertical take-off through high-frequency flapping motion [1], [2], most of large flapping wing birds realize the take-off via jumping. Previous research has proved that leg thrust plays a primary role in taking off [3]–[7].

Besides jumping, rotor and running take-offs have been explored for FWAVs. As a popular form of aerial robots, quadrotors can easily realize vertical take-off and hovering.

This work was supported by the Natural Science Foundation of China(NSFC) under the Grant 52022056 and 52205031.(*Corresponding author: Genliang Chen.*)

Wei Yan, Genliang Chen and Hao Wang are with the State Key Laboratory of Mechanical Systems and Vibration, Shanghai Jiaotong University, Shanghai, China(email: ywgump@sjtu.edu.cn; leungchan@sjtu.edu.cn; wanghao@sjtu.edu.cn)

Wei Yan and Zhuang Zhang are with School of Engineering, Westlake University, Hangzhou, Zhejiang, 310030, China (email: zhangzhuang@westlake.edu.cn)

Fig. 1. The complete process of jumping take-off.

Some researchers combine the quadrotor with FWAV [8]. The robot can utilize a quadrotor to reach the specific height and switch to the flapping flight. However, the arrangement of the quadrotor has an aerodynamic influence on the flapping wing. In addition, the energy efficiency of the rotor is low which is opposed to the intention of the flapping wing.

Another approach to take-off is running take-off. Similar to the airplane, the wheeled landing gear can be installed on the FWAV [9]. Through the flapping motion, FWAV can accelerate to the take-off velocity and switch to the flapping flight. Except for wheels, some researchers attach bipedal legs on FWAV which can gain high-speed running and transfer from terrestrial mode to aerial mode [10]. Since the running take-off needs a certain running distance on the ground, the flatness of the take-off place must be considered. In addition, the flapping motion during running also influences the stability of robot. The above two weaknesses limit the application of running take-off.

In contrast, jumping take-off offers versatility across terrains without the need for a run-up. It is also energetically efficient as the elastic energy used can be stored gradually. In addition, the jumping legs have less aerodynamic influence than the supplement of rotors. However, most of current researches focus on leg mechanisms and simulations [11]–[14], with no real-world FWAVs demonstrating this capability.

Considering the design in previous research, realizing a jumping take-off in FWAVs presents two significant challenges:

1) Structural weight: Existing designs often require complex leg mechanisms and multiple actuators, increasing overall weight. This directly affects jumping efficiency and in-flight maneuverability.
2) Stable transition: The sudden motion of jumping can drastically alter the robot's attitude. However, flapping flight has a high demand on the angle of attack (AOA) to obtain enough lift and avoid stalling. Thus, it is necessary to maintain an ideal attitude during the jumping

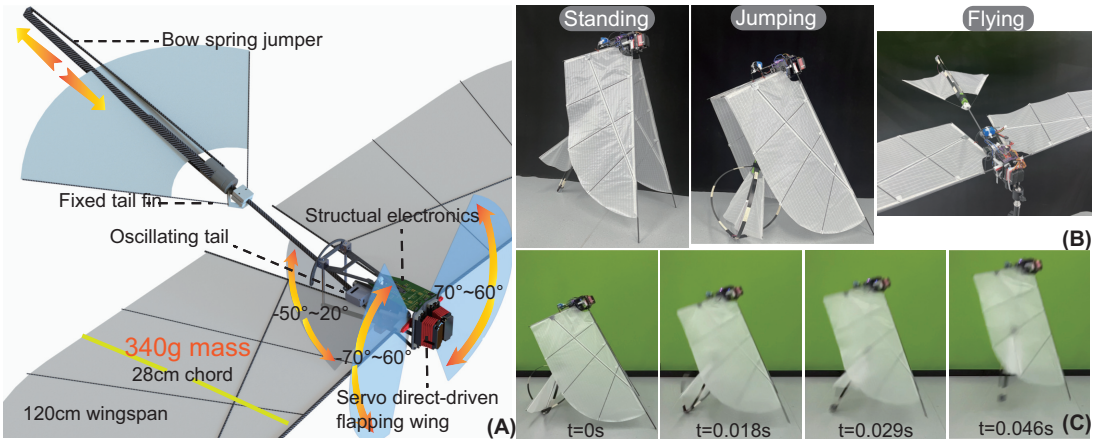

Fig. 2. Overview of mechanical design (a) Four degrees of freedom and necessary feature in mechanical design, including two independently-driven flapping wing, an active oscillating tail and the compression of bow spring jumper. (b)Three different modes in the process of jumping take-off: standing mode (two wings and the tail act as a tripod-like structure), jumping mode (the bow spring jumping is compressed), flying mode (two wings and the tail flap upward) (c)Sequential frame of the on-ground jumping phase. Time is less than 0.1s from release to off the ground.

and transition phases.

In this paper, we propose a novel structure of FWAV capable of jumping take-off from flat ground. The robot has a lightweight structure, with a wingspan of 1.2m and a weight of 340g. The flapping wings are directly driven by two servos. The carbon fiber spring is employed to build a light-weight jumping module with high elastic energy. According to the specific structure, we build the dynamic model of the jumping take-off process. Through analyzing the aerodynamic effect in the process, we realize a stable transition from ground standing to aerial flying. Fig.1 shows the complete process of jumping take-off which is the first successful jumping take-off of a meter-scale FWAV. In brief, this paper discusses the structure, dynamic modeling, and detailed implementation to perform a jumping take-off

II. Mechanical Design

The primary consideration of mechanical design is the realization and arrangement of jumping mechanism and flapping wing. A comprehensive depiction of the structure can be found in Fig.2(a). The whole system has four degrees of freedom. It is equipped with two flapping wings, each controlled by its own servo. Additionally, a bow-spring jumper is incorporated to accumulate elastic energy via compression. An active joint, located between the robot's body and tail, allows the robot to transfer from steady standing to flying, as shown in Fig.2(b).

A. Switch between the jumping mode and flapping mode

The proposed design can be divided into three parts: the main body, the tail component, and two separate wings. The tail component, which includes the tail fin and the jumping mechanism, is connected to the main body through an active revolute joint whose motion range is $-50^\circ - 20^\circ$. Steady standing is the primary requirement of jumping mode. Fig.2(b) exhibits three different states of the robot: standing mode, jumping mode, and flying mode. In the standing mode, two separate wings and the tail component act as a tripod-like structure to support the main body. Through compressing the jumping mechanism, the elastic energy can be stored to realize the jumping motion. Compared to the birds in nature which perform a standing jump with two legs, the present design has a lower mechanical complexity, which eliminates the balance control and reduces the number of actuators. The wing surface is kept close to the main body during the ascending phase. Low exposed wing area can efficiently reduce the drag force and improve the jump height. When the robot reaches the apex, the tail component and two wings flap upward and transfer to flying mode.

B. Servo direct-driven flapping wing

As shown in Fig.2(b), two wings flap near the horizontal plane in flying mode and maintain a low position in standing and jumping modes. To be compatible with two different motions, both wings need to have a large range of motion. Traditional flapping motion depends on a single motor and the transmission mechanism, which can convert a continuous rotation into a reciprocating flapping [15]. This method can synchronize the flapping motion of two wings and only generate a constant-amplitude motion near the horizontal plane. To overcome the limitation, we use two actuators to independently control two wings. Such a controlling form of FWAV has been validated in the previous research [16]. Independent wing control allows the phase position of wings to be freely adjusted and enables a successful switch between two modes at the mechanical level. In the proposed design, the motion range is between -60° and 70°.

Flight attitude and altitude control are critical capabilities for FWAV. For traditional FWAVs with synchronous flapping motion, an active rudder and elevator on the tail are necessary for pitch and yaw control. By contrast, our design can realize flight control only relying on the independently controlled wings, in other words, with a fixed tail wing. The realization of pitch and yaw control can be achieved through co-

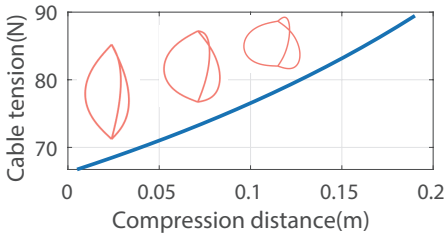

Fig. 3. Force-deflection behaviour of bow spring jumper. Red line denotes the deformable state.

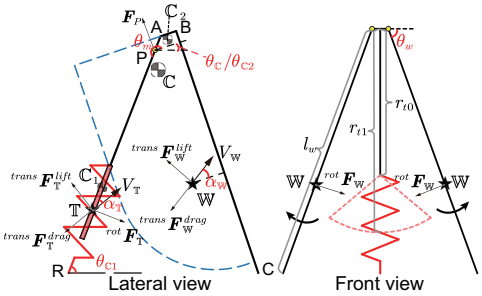

Fig. 4. A schematic annotated with force condition and key geometric parameters for dynamic modeling. Red spring, red dashed line and blue dashed line respectively denote the jumping mechanism,tail fin and wings.

directional or counter-directional adjustments to the wings' equilibrium positions. The detailed control strategy can be referred to [17].

The payload of the flapping wing module is also significant in the proposed design due to the additional weight of the jumping mechanism. We designed the flapping wing with a wingspan of 1.2m and a mean chord length of 260mm. To supply enough torque to drive the flapping wing, we select two KST X15-1809 as wing actuators, achieving a 70° amplitude and 3Hz flapping frequency motion.

C. Jumping module composed of three bow springs

Due to the payload of the flapping wing and the requirement of jumping height, the main demand of the jumping module is high energy density, which means high elastic energy and lightweight. Referring to the design in [18], the carbon fiber bow spring is employed to store the elastic energy for jumping take-off. Three carbon fiber springs are symmetrically distributed and connected with each other through the nylon hinge at both ends. The PE (Polyethylene) fishing line is fixed at the distal end to realize energy storage and release. The active revolute joint can adjust the launch angle and realize the transition from jumping to flying.

The length, width, and thickness of the carbon fiber spring are respectively 370mm, 10mm, and 1.5mm. Based on our previous method on the modeling of flexible beam [19], the force-deflection behavior and corresponding deformation state are shown in Fig.3. The elastic energy after full compression is approximately 8.5J. Considering the mass of 340g and the energy loss due to the air drag, 8.5J of elastic energy is enough to generate 1.5m of jumping height for the take-off. The launching mechanism can be referred to [20], which can relaunch several times without human intervention.

III. Planar Dynamic Model

In the dynamic modeling, we make a simplifying assumption: the two wings are always arranged symmetrically and exhibit synchronous motion. This implies that the aerodynamic forces acting on both wings are identical. With this assumption, the dynamic process of the jumping take-off is effectively reduced to a planar model. The entire take-off process is divided into two distinct phases: the 'jumping phase,' where the tail and both wings hang down to form a tripod-like structure, and the 'transition phase,' during which the tail and wings flap upward and transfer into a flapping mode. Based on the dynamic model, we proceed to analyze the impact of aerodynamic forces in each of the two phases. Combining the experimental validation, the method to realize a stable transition is introduced in this section.

A. Modeling of the jumping phase

The jumping phase can be further divided into two parts: on the ground and off the ground. When on the ground, the jumper stores the elastic energy via compression and realizes the jumping motion through instantaneous release. To avoid slippage on the ground, we set a large launch angle($\theta_{\mathbb{C}_1}$) towards the vertical direction. Due to the alignment between the spring force line and the center of mass (CM), the robot undergoes a nose-down rotation after leaving the ground. For simplicity, the on-ground jumping process is approximated by specifying the initial linear and angular velocity when leaving the ground.

When off the ground, we treated the robot as a whole body. As shown in Fig.4, the CM is a fixed point named $\mathbb{C}$. $\mathbb{T}$ and $\mathbb{W}$ are the aerodynamic center (AC) of the tail fin and wings. The Newton-Euler equations can be written as:

$$\begin{aligned} m_{\mathbb{C}}\ddot{\boldsymbol{r}}_{\mathbb{C}} &= m_{\mathbb{C}}\boldsymbol{g} + \boldsymbol{F}_{\mathbb{T}} + \boldsymbol{F}_{\mathbb{W}} \\ I_{\mathbb{C}}\ddot{\theta}_{\mathbb{C}} &= \boldsymbol{r}_{\mathbb{C},\mathbb{T}} \times \boldsymbol{F}_{\mathbb{T}} + \boldsymbol{r}_{\mathbb{C},\mathbb{W}} \times \boldsymbol{F}_{\mathbb{W}} \end{aligned} \tag{1}$$

in which $m_{\mathbb{C}}, I_{\mathbb{C}}$ are the mass and inertia of the robot, $\boldsymbol{r}_{\mathbb{C}}, \theta_{\mathbb{C}}$ are the position vector and pitch angle, $\boldsymbol{r}_{\mathbb{C},\mathbb{W}}$ represents the vector pointing from $\mathbb{C}$ to $\mathbb{W}$, $\boldsymbol{g}$ is gravitational acceleration. $\boldsymbol{F}_{\mathbb{W}}$ and $\boldsymbol{F}_{\mathbb{T}}$ are aerodynamic force applied on the wing and tail fin,include lift ${}^{trans}\boldsymbol{F}^{lift}_{\mathbb{W}/\mathbb{T}}$ and drag ${}^{trans}\boldsymbol{F}^{drag}_{\mathbb{W}/\mathbb{T}}$:

$$\begin{aligned} {}^{trans}\boldsymbol{F}^{lift}_{\mathbb{W}/\mathbb{T}} &= \tfrac{1}{2}\rho C^{L}_{\mathbb{W}/\mathbb{T}} V^{2}_{\mathbb{W}/\mathbb{T}} S_{\mathbb{W}/\mathbb{T}} \\ {}^{trans}\boldsymbol{F}^{drag}_{\mathbb{W}/\mathbb{T}} &= \tfrac{1}{2}\rho C^{D}_{\mathbb{W}/\mathbb{T}} V^{2}_{\mathbb{W}/\mathbb{T}} S_{\mathbb{W}/\mathbb{T}} \end{aligned} \tag{2}$$

where ρ is the air density. $V_{\mathbb{T}/\mathbb{W}} = \dot{\boldsymbol{r}}_{\mathbb{C}} + \boldsymbol{r}_{\mathbb{C},\mathbb{W}/\mathbb{T}} \times \dot{\theta}_{\mathbb{C}}$ denotes the velocity of AC. $S_{\mathbb{W}/\mathbb{T}}$ is the area of aerodynamic surface in which $S_{\mathbb{W}} = S_{\mathbb{W},actual} cos(\theta_w)$ is approximated as the projected area of the actual wing area $S_{\mathbb{W},actual}$ in the plane of main body, and $S_{\mathbb{T}}$ is area of tail fin. C^L and C^D are respectively lift and drag coefficient [21].

$$C^L = 2sin(\alpha)cos(\alpha) \quad C^D = 2sin^2(\alpha) \tag{3}$$

in which α is the AOA of aerodynamic surface. The Equ.1 is an ordinary differential equation(ODE) and can be directly solved by ode45() in MATLAB.

TABLE I

AERODYNAMIC INFLUENCE AT JUMPING PHASE

	Average Height(m)	**Pitch angle at apex**(°)
W.w&t	1.602	22.65
W.w	1.707	35.72
W.t	1.906	1.04
W.O.w&t	1.786	-135.45

B. Implications of aerodynamic force during the jumping phase

Both the wings and the tail fin are subjected to aerodynamic forces during the jumping phase. To individually analyze the aerodynamic impact of the wings and the tail fin, we categorize the configurations into four conditions:

1) With both wings and tail fin (denoted as W.w&t)
2) With only wings (denoted as W.w)
3) With only the tail fin (denoted as W.t)
4) Without either wings or tail fin (denoted as W.O.w&t)

To capture the robot's motion, we employed the Optitrack Prime13 system. By attaching markers to the robot's body, we were able to record both the jumping height and the pitch angle during the jumping phase. To improve accuracy, every condition is measured three times. The average value of maximum height and pitch angle are shown in Table. I.

Comparing the jumping height among four conditions, both the tail fin and wing will cause a height loss. The complete robot with wings and tail fin can achieve nearly 1.6m of jumping height, which is enough for a transition. Thus, we pay more attention to the difference in pitch angle among the four conditions. In the absence of any aerodynamic surfaces, the robot undergoes obvious nose-down rotation upon leaving the ground. The phenomenon is caused by the misalignment between CM ($\mathbb{C}$) and the elastic force line *PR*. The inclusion of either wings or a tail fin helps reduce this rotation, allowing the robot to maintain a nearly horizontal attitude until reaching the apex. The corresponding video can be seen in the supplementary material.

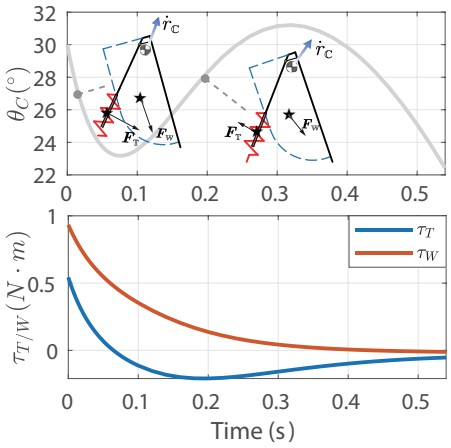

Fig. 5. Simulation results during jumping phase with both wings and tail fin. (a)Temporal variation curves of the robot's pitch angle and its force conditions at 0.02s and 0.2s (b)Temporal variation curves of torque about CM generated by aerodynamic force $\boldsymbol{F}_{\mathbb{T}}$ and $\boldsymbol{F}_{\mathbb{W}}$.

To investigate the reasons for resisting nose-down rotation, we simulated the torque generated by aerodynamic forces on both the tail fin and wings during the jumping phase. The mass and inertia of robot are set as $m_{\mathbb{C}} = 0.34kg, I_{\mathbb{C}} = 1.54 \times 10^{-2} kg \cdot m^2$. Other initial values are set as:$\theta_{\mathbb{C}} = 30^\circ, \ddot{\theta}_{\mathbb{C}} = -4rad/s, \ddot{\boldsymbol{r}}_{\mathbb{C}} = [2.7, 7.5]m/s$.

As shown in Fig. 5, $M_{\mathbb{T}}$ and $M_{\mathbb{W}}$ denote the torques about the CM generated by $\boldsymbol{F}_{\mathbb{T}}$ and $\boldsymbol{F}_{\mathbb{W}}$ respectively. Although both the tail fin and wings contribute to resisting nose-down rotation, they operate based on distinct principles. The wing surface is nearly orthogonal to the moving direction $\dot{\boldsymbol{r}}_{\mathbb{C}}$, resulting in $M_{\mathbb{W}}$ always being a nose-up torque, suitable for compensating only nose-down rotation. In contrast, the tail fin is aligned parallel to $\dot{\boldsymbol{r}}_{\mathbb{C}}$, with its center of pressure (CP) placed behind the CM. Similar to the principle of rocket fins, the tail fin offers dynamic stability, whether the robot undergoes a nose-down or nose-up rotation. When the robot tilts away from its intended trajectory, the air will flow over the tail fin at an angle, generating the lift force. The lift force will push the robot back in line. It's worth noting that dynamic stability is achieved during high-speed motions. As the upward velocity diminishes, the robot exhibits a gradual nose-down rotation, indicated by a decrease in $\theta_{\mathbb{C}}$.

C. Modeling of transition phase

When the robot reaches its apex, the transition phase begins. During this phase, the tail and the two wings execute an upstroke, influencing the attitude of the robot. Given that the wings are lightweight and their CM is close to $\mathbb{C}$ along the chordwise, the inertial force they exert on pitching motion is negligible. Consequently, the aerodynamic force acting on the wings is assumed to have a direct effect on the main body. As such, the system is modeled as comprising only two primary components: the tail component (comprising the tail fin and jumper) and the body part (including the main body and two wings), whose CM are respectively denoted by $\mathbb{C}_1$ and $\mathbb{C}_2$ respectively.The Newton-Euler equations governing the dynamics of these two bodies are as follows:

$$\mathbf{M}\ddot{\boldsymbol{x}} = \boldsymbol{F}_e + \mathbf{Q}\boldsymbol{\lambda} \tag{4}$$

With

$$\begin{aligned}
&\mathbf{M} = diag\{m_{\mathbb{C}_1} m_{\mathbb{C}_1} I_{\mathbb{C}_1} m_{\mathbb{C}_2} m_{\mathbb{C}_2} I_{\mathbb{C}_2}\} \\
&\ddot{\boldsymbol{x}} = \begin{bmatrix} \ddot{\boldsymbol{r}}_{\mathbb{C}_1} & \ddot{\theta}_{\mathbb{C}_1} & \ddot{\boldsymbol{r}}_{\mathbb{C}_2} & \ddot{\theta}_{\mathbb{C}_2} \end{bmatrix}^T \\
&\boldsymbol{F}_e = \begin{bmatrix} m_{\mathbb{C}_1}\boldsymbol{g} + \overline{\boldsymbol{F}_{\mathbb{T}}} \\ \boldsymbol{r}_{\mathbb{C}_1,\mathbb{T}} \times \overline{\boldsymbol{F}_{\mathbb{T}}} - \tau_P \\ m_{\mathbb{C}_2}\boldsymbol{g} + \overline{\boldsymbol{F}_{\mathbb{W}}} \\ \boldsymbol{r}_{\mathbb{C}_2,\mathbb{W}} \times \overline{\boldsymbol{F}_{\mathbb{W}}} + \tau_P \end{bmatrix} \\
&\boldsymbol{\lambda} = \boldsymbol{F}_P \\
&\mathbf{Q} = \begin{bmatrix} \mathbf{E}_{2\times 2}, & \boldsymbol{r}_{\mathbb{C}_1,P}\times, & -\mathbf{E}_{2\times 2}, & \boldsymbol{r}_{\mathbb{C}_2,P}\times \end{bmatrix}^T
\end{aligned} \tag{5}$$

$\mathbf{M}$ is an inertial matrix in which $m_{\mathbb{C}_1}, m_{\mathbb{C}_2}, I_{\mathbb{C}_1}, I_{\mathbb{C}_2}$ are the mass and inertia of tail component and body about respective

CM. $\boldsymbol{r}_{\mathbb{C}_1}, \theta_{\mathbb{C}_1}, \boldsymbol{r}_{\mathbb{C}_2}, \theta_{\mathbb{C}_2}$ in $\boldsymbol{x}$ are the position vector and pitch angle. $\boldsymbol{F}_P$ and τ_P are the constraint force and driving torque at the revolute joint. $\overline{\boldsymbol{F}_{\mathbb{W}}}$ and $\overline{\boldsymbol{F}_{\mathbb{T}}}$ are aerodynamic force applied on the wing and tail fin, which include two parts: ${}^{trans}\boldsymbol{F}_{\mathbb{W}/\mathbb{T}}$ that is generated by the translational motion, ${}^{rot}\boldsymbol{F}_{\mathbb{W}/\mathbb{T}}$ due to the upstroke during transition. ${}^{trans}\boldsymbol{F}_{\mathbb{W}/\mathbb{T}}$ can be directly obtained via Equ.2. ${}^{rot}\boldsymbol{F}_{\mathbb{W}}$ and ${}^{rot}\boldsymbol{F}_{\mathbb{T}}$ can be respectively acquired through integrating along the spanwise and the length of tail :

$$\begin{aligned} {}^{rot}\boldsymbol{F}_{\mathbb{W}} &= \int_0^{l_w} \tfrac{1}{2}\rho C^D_{90^\circ}\dot{\theta}_w^2 c(r_w) r_w^2\, dr_w \\ {}^{rot}\boldsymbol{F}_{\mathbb{T}} &= \int_{r_{t0}}^{r_{t1}} \tfrac{1}{2}\rho C^D_{90^\circ}\dot{\theta}_m^2 c(r_t) r_t^2\, dr_t \end{aligned} \tag{6}$$

In which $C^D_{90^\circ} = 2$ denotes the drag coefficient when AOA$=90^\circ$,r_w and r_t are the respective radial lengths along the wing span and from the tail fin to point P. $c(r_t)$ and $c(r_w)$ are the corresponding chord length at r_t and r_w.The system has four degrees of freedom (DOF). To simplify the model, the location of main body $\boldsymbol{r}_{\mathbb{C}_2}$, pitch angle of tail component $\theta_{\mathbb{C}_1}$ and the angle of active revolute joint θ_m are selected as the generalized coordinates $\boldsymbol{q} = [\boldsymbol{r}_{\mathbb{C}_2}\ \theta_{\mathbb{C}_1}\ \theta_m]$. $\boldsymbol{x}$ can be expressed with $\boldsymbol{q}$

$$\boldsymbol{x} = \boldsymbol{x}(q) \tag{7}$$

Taking the first and second-order derivatives of the above equation, $\dot{\boldsymbol{x}}$ and $\ddot{\boldsymbol{x}}$ can be denoted as:

$$\dot{\boldsymbol{x}} = \mathbf{J}_{xq}\dot{\boldsymbol{q}} \quad \ddot{\boldsymbol{x}} = \mathbf{J}_{xq}\ddot{\boldsymbol{q}} + \dot{\mathbf{J}}_{xq}\dot{\boldsymbol{q}} \tag{8}$$

$\mathbf{J}_{xq}$ is the Jacobian matrix reflecting $\dot{\boldsymbol{x}}$ to $\dot{\boldsymbol{q}}$. Substituting into, they can be rewritten into:

$$\mathbf{M}\mathbf{J}_{xq}\ddot{\boldsymbol{q}} + c(\boldsymbol{q},\dot{\boldsymbol{q}}) = \boldsymbol{F}_e + \mathbf{Q}\boldsymbol{\lambda} \tag{9}$$

in which $c(\boldsymbol{q},\dot{\boldsymbol{q}}) = \mathbf{M}\dot{\mathbf{J}}_{xq}\dot{\boldsymbol{q}}$ is a function about $\boldsymbol{q},\dot{\boldsymbol{q}}$. Based on d'Alembert's principle, the motion equations of the system can be expressed as an ordinary differential equation(ODE) via premultiplicating $\mathbf{J}_{xq}^T$ [22]:

$$\mathbf{J}_{xq}^T\mathbf{M}\mathbf{J}_{xq}\ddot{\boldsymbol{q}} + \mathbf{J}_{xq}^T c(\boldsymbol{q},\dot{\boldsymbol{q}}) = \mathbf{J}_{xq}^T\boldsymbol{F}_e \tag{10}$$

Through substituting the known trajectory of the active revolute joint(θ_m), the Equ.10 can be transferred into DAE which can be solved by ode15s() in Matlab.

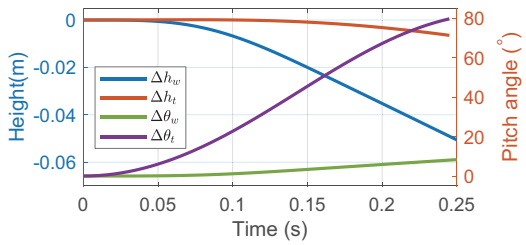

Fig. 6. The influence of the tail and wing's upstroke on the height and pitch angle.Δh_w and Δh_t respectively are the height changes during the wing and tail's upstroke. $\Delta\theta_w$ and $\Delta\theta_t$ respectively are the variation of $\theta_{\mathbb{C}_2}$ during wing and tail's upstroke.

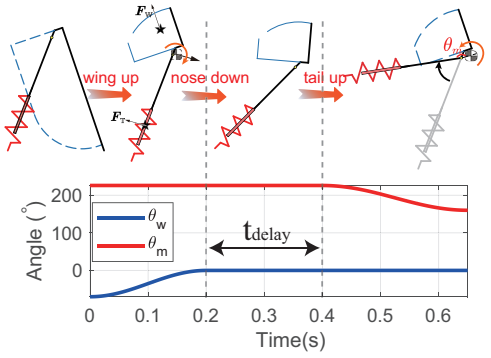

Fig. 7. Progress of delayed stroke: the wings flap upward→nose-down rotation (caused by $\boldsymbol{F}_{\mathbb{W}}$ and $\boldsymbol{F}_{\mathbb{T}}$)→ the tail flaps upward→ nose-up rotation (caused by inertia of tail component).

D. Influence of wing and tail's upstroke

In the transition phase from jumping to flight, both the wings and tail components execute an upstroke, having an influence on the pitch angle and altitude of the robot. We independently examined the effects of the upstroke motion of both the tail and wing. During the simulation, we neglect the aerodynamic force induced by translational motion and gravity acceleration. Thus, we initialized the velocity of CM, $\dot{\boldsymbol{r}}_{\mathbb{C}2}$, to be $[0,0]m/s$ and the angular velocity, $\dot{\theta}_{\mathbb{C}_2}$, to be $0rad/s$. The mass and inertia of the main body and tail component is set as:$m_{\mathbb{C}_2} = 0.26kg, m_{\mathbb{C}_1} = 0.08kg, I_{\mathbb{C}_2} = 4\times10^{-4}kg\cdot m^2, I_{\mathbb{C}_2} = 1.8\times10^{-3}kg\cdot m^2$. Furthermore, the angle trajectories for θ_m (relative motion between the main body and tail component) and θ_w (corresponding to wing motion) are modeled using sinusoidal waves as shown in Fig.7. The results of our simulations are presented in Fig.6.

Our findings indicate that the influence of tail component and wings' upstroke on the robot's altitude are nearly 0.01m and 0.05m, being negligible. Because the AC of the wing, is in close proximity to the CM, the upstroke of two wings exerts a limited impact on the pitch angle. In contrast, the tail, with its considerable inertia, induces a substantial nose-up rotation (about 80° increase of $\theta_{\mathbb{C}_2}$).

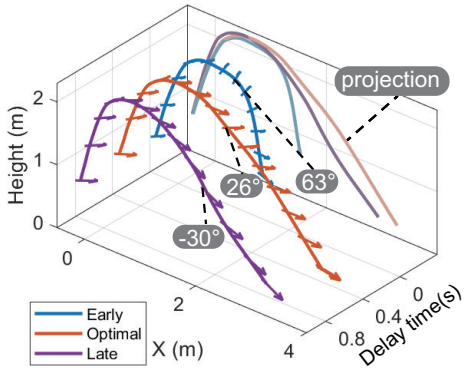

Fig. 8. The trajectory under different delayed time($t_{delay} = 0, 0.4, 0.8s$) is shown. The arrow on the trajectory represents the pitch angle. The pitch angle after transition is respectively $63^\circ, 26^\circ, -30^\circ$,

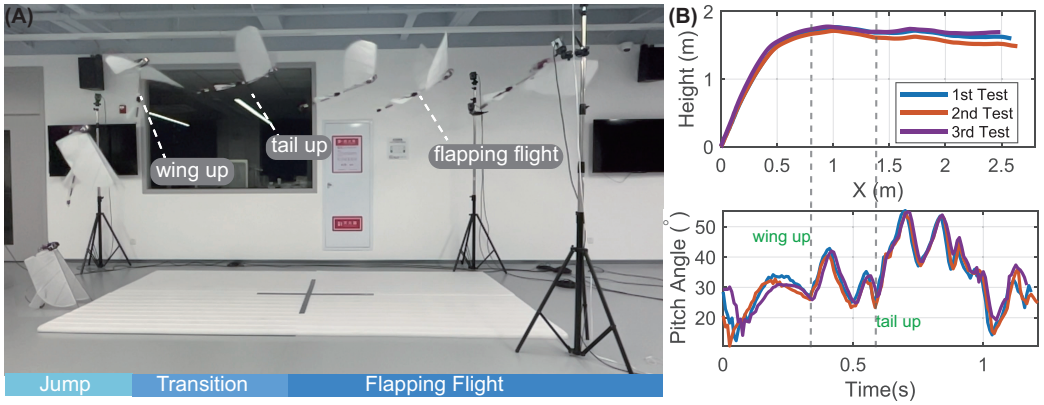

Fig. 9. Complete process of jumping take-off. (a)Sequential frames from the video of the jumping take-off process. (tripod-like stand→jumping off the ground→wing up→tail up→flapping flight) (b)The trajectory and variation of pitch angle in the process during three tests.

E. Realization of stable transition

For optimal aerodynamic performance, the robot should maintain a slight positive AOA after transition. An AOA within the range of $\theta_{\mathbb{C}_2} = 0 - 40^\circ$ ensures adequate lift for sustained flight. Exceeding this range may result in a stall, compromising loss of both control and altitude. A negative AOA diminishes lift, causing a significant altitude drop.

The preceding section identifies the tail's upstroke as the primary factor influencing attitude change, often causing significant nose-up rotation. To mitigate this, we introduce the "delayed upstroke" strategy. As illustrated in Fig. 7, both wings flap upward initially at the apex, followed by the tail's upstroke after a predefined delay t_{delay}. This delay enhances the nose-down rotation caused by $\boldsymbol{F}_{\mathbb{W}}$ and $\boldsymbol{F}_{\mathbb{T}}$, induced by the translational velocity $\dot{\boldsymbol{r}}_{\mathbb{C}2}$, counterbalancing the nose-up rotation during the tail's upstroke. Subsequently, the tail ascends, achieving a desirable AOA for a flapping fight.

The selection of t_{delay} is crucial. A too-short t_{delay} under-compensates the nose-up rotation, while an excessively long t_{delay} results in a negative AOA post-transition. Our jump-glide experiments, with varying t_{delay}, capture $\theta_{\mathbb{C}_2}$'s fluctuations. Precise control of delay time relies on the positioning system. When the robot approaches the apex, the Optitrack system on the upper computer will send the signal to the control board through the wireless serial module, triggering the upward wing. The timers on the control board will record t_{delay} and then trigger the upward tail motion. As depicted in Fig. 8, for $t_{delay} = 0$, the resultant $\theta_{\mathbb{C}_2}$ of 63° induces a stall. For $t_{delay} = 0.8s$, $\theta_{\mathbb{C}_2}$ is -30°, leading to a nose dive. In contrast, a t_{delay} of 0.4s yields a stable post-transition attitude, registering $\theta_{\mathbb{C}_2}$ at 26° (refer to the supplementary video for detailed trajectories).

IV. Experimental Validation

In the previous section, we revealed the principle of a stable jumping attitude and introduced the 'delayed stroke' approach for a stable transition from jumping to flying. In this section, we made three attempts at jumping take-off to validate the feasibility of the proposed method. The physical picture of jumping take-off is shown in Fig.9(A), while Fig.9(B) illustrates the corresponding pitch angle and trajectory. The robot consistently maintains stability during its jumping phase. At the apex, two wings flap upward first, accompanied by an approximate 10° nose-up rotation. Different from the jump-glide motion in Fig.8, to maintain the altitude, the wings will subsequently initiate a flapping motion after the upstroke. The thrust force induced by the flapping wing will increase the forward velocity, thereby enhancing the nose-down torque. Thus, the delayed time of the tail's upstroke is set as 0.3s, shorter than 0.4s in jump-glide motion. After a delayed time, the tail's upstroke induced a 30° nose-up rotation, achieving a positive AOA for flapping flight. The payload of flapping motion is enough to support self-weight and maintain a constant altitude flight. The differences in the motion trajectories and pitch angle variations across three attempts are minimal, verifying the robustness of the system.

V. Conclusion and Future Work

In this paper, we demonstrated the first successful jumping take-off of FWAV. Our design combines a servo direct-driven FWAV with a carbon-fiber spring jumper. With a low mechanical complexity, the robot is lightweight at just 340g, enabling it to jump nearly 1.7m and also accommodate the payload requirements for flapping flight. Based on a specific structure, we developed a dynamic model covering both the jumping and transition phases. During the jumping phase, the tail fin acts as a stabilizer to help the robot stay level until it reaches the apex. We have also introduced a delayed-stroke method (where the wings flap upward when the robot is at the apex, followed by the tail starting its motion after a set delay) to ensure a smooth transition from jumping to flying. Finally, we validated the system's stability through three jumping take-off tests.

The proposed method of stable transition requires very precise timing in the tail actuation, which limits its adaptability in different external conditions. In the future, we plan to focus on improving the robot's sensing and control to perform autonomous jumping take-offs on varied terrains in an outdoor environment.

REFERENCES

[1] M. Keennon, K. Klingebiel, and H. Won, "Development of the nano hummingbird: A tailless flapping wing micro air vehicle," in *AIAA Aerosp. Sci. Meet. Incl. New Horiz. Forum Aerosp. Expo.*, 2012, p. 588.

[2] B. W. Tobalske, D. L. Altshuler, and D. R. Powers, "Take-off mechanics in hummingbirds (trochilidae)," *J. Exp. Biol.*, vol. 207, no. 8, pp. 1345–1352, 2004.

[3] R. H. Bonser and J. M. Rayner, "Measuring leg thrust forces in the common starling," *J. Exp. Biol.*, vol. 199, no. 2, pp. 435–439, 1996.

[4] B. Parslew, G. Sivalingam, and W. Crowther, "A dynamics and stability framework for avian jumping take-off," *R. Soc. Open Sci.*, vol. 5, no. 10, p. 181544, 2018.

[5] K. D. Earls, "Kinematics and mechanics of ground take-off in the starling sturnis vulgaris and the quail coturnix coturnix," *J. Exp. Biol.*, vol. 203, no. 4, pp. 725–739, 2000.

[6] F. H. Heppner and J. G. Anderson, "Leg thrust important in flight take-off in the pigeon," *J. Exp. Biol.*, vol. 114, no. 1, pp. 285–288, 1985.

[7] P. Provini, B. W. Tobalske, K. E. Crandell, and A. Abourachid, "Transition from leg to wing forces during take-off in birds," *J. Exp. Biol.*, vol. 215, no. 23, pp. 4115–4124, 2012.

[8] D. Ma, B. Song, Z. Wang, J. Xuan, and D. Xue, "Development of a bird-like flapping-wing aerial vehicle with autonomous take-off and landing capabilities," *J. Bionic Eng.*, vol. 18, pp. 1291–1303, 2021.

[9] J. H. Kim, C. Y. Park, S. Jun, D. K. Chung, J. R. Kim, H. C. Hwang, B. Stanford, P. Beran, G. Parker, and D. Mrozinski, "Flight test measurement and assessment of a flapping micro air vehicle," *Int. J. Aeronaut. Space Sci.*, vol. 13, no. 2, pp. 238–249, 2012.

[10] K. Peterson and R. S. Fearing, "Experimental dynamics of wing assisted running for a bipedal ornithopter," in *IEEE Int Conf Intell Rob Syst*. IEEE, 2011, pp. 5080–5086.

[11] J. Zhang, C. Dong, and A. Song, "Jumping aided takeoff: Conceptual design of a bio-inspired jumping-flapping multi-modal locomotion robot," in *IEEE Int. Conf. Robot. Biomimetics, ROBIO*. IEEE, 2017, pp. 32–37.

[12] O. A. Hudson, M. Fanni, S. M. Ahmed, and A. Sameh, "Autonomous flight take-off in flapping wing aerial vehicles," *J. Intell. Robot. Syst.*, vol. 98, pp. 135–152, 2020.

[13] D. Ma, B. Song, D. Xue, and J. Xuan, "Conceptual design of bio-inspired jumping mechanisms for flapping-wing aerial vehicles," *China Mech. Eng.*, vol. 33, no. 15, p. 1869, 2022.

[14] G. Sivalingam, *Design of Jumping Legs for Flapping Wing Vehicles*. The University of Manchester (United Kingdom), 2017.

[15] C. Zhang and C. Rossi, "A review of compliant transmission mechanisms for bio-inspired flapping-wing micro air vehicles," *Bioinspir. Biomim.*, vol. 12, no. 2, p. 025005, 2017.

[16] J. Gerdes, A. Holness, A. Perez-Rosado, L. Roberts, A. Greisinger, E. Barnett, J. Kempny, D. Lingam, C.-H. Yeh, H. A. Bruck, *et al.*, "Robo raven: a flapping-wing air vehicle with highly compliant and independently controlled wings," *Soft Robot.*, vol. 1, no. 4, pp. 275–288, 2014.

[17] H. Huang, W. He, J. Wang, L. Zhang, and Q. Fu, "An all servo-driven bird-like flapping-wing aerial robot capable of autonomous flight," *IEEE-ASME Trans. Mechatron.*, vol. 27, no. 6, pp. 5484–5494, 2022.

[18] E. W. Hawkes, C. Xiao, R.-A. Peloquin, C. Keeley, M. R. Begley, M. T. Pope, and G. Niemeyer, "Engineered jumpers overcome biological limits via work multiplication," *Nature*, vol. 604, no. 7907, pp. 657–661, 2022.

[19] W. Yan, G. Chen, S. Tang, Z. Zhang, X. Duan, and H. Wang, "Design of a reconfigurable planar parallel continuum manipulator with variable stiffness," in *Lect. Notes Comput. Sci.* Springer, 2021, pp. 803–813.

[20] G.-P. Jung, C. S. Casarez, S.-P. Jung, R. S. Fearing, and K.-J. Cho, "An integrated jumping-crawling robot using height-adjustable jumping module," in *IEEE Int. Conf. Robot. Autom.*, 2016, pp. 4680–4685.

[21] R. Cory and R. Tedrake, "Experiments in fixed-wing uav perching," in *AIAA Guid., Navig. Control Conf. Exhib.*, 2008, p. 7256.

[22] W. Schiehlen, "Multibody system dynamics: roots and perspectives," *Multibody Syst. Dyn.*, vol. 1, pp. 149–188, 1997.